



Article

Simultaneous Photocatalytic CO_2 Reduction and Methylene Blue Degradation over $TiO_2@(Pt, Au, or Pd)$

Elisenda Pulido-Melián *D, Cristina Valeria Santana-Fleitas, Javier Araña and Óscar Manuel González-Díaz *D

Grupo de Fotocatálisis y Espectroscopía para Aplicaciones Medioambientales, Instituto Universitario de Estudios Ambientales y Recursos Naturales (i-UNAT), Universidad de Las Palmas de Gran Canaria, 35017 Las Palmas, Spain; cristina.santana145@alu.ulpgc.es (C.V.S.-F.); javier.arana@ulpgc.es (J.A.)

* Correspondence: elisenda.pulido@ulpgc.es (E.P.-M.); oscar.gonzalez@ulpgc.es (Ó.M.G.-D.)

Abstract

In this work, the photocatalytic reduction of CO_2 was innovatively tested with the simultaneous removal and mineralization of a textile contaminant, methylene blue (MB), which acts as a sacrificial agent. The process was carried out in a flow regime under atmospheric conditions, using a liquid-phase photoreactor under UVA illumination with a duration of 24 h per test. Two commercial TiO_2 -based photocatalysts, P25 and P90 from Evonik, were used and surface modified through the photodeposition of metallic nanoparticles of Pt, Au, and Pd, as they did not show gas-phase products from CO_2 reduction on their own. The optimal pH was 5, the decreasing order of activity by metal was Pt > Au > Pd, and the optimal MB concentration was 20 ppm. The major products were CH_4 and H_2 in the gas phase. The presence of CH_4 was only detected in the presence of a CO_2 flow. In the liquid phase, carboxylic acids were also detected in small amounts, and in the test, 100 ppm of MB ethanol was additionally detected. A 100% degradation of MB and 72.5% mineralization was achieved under the conditions of highest CH_4 production (20 ppm MB at pH 5 with $4 \text{ g} \cdot \text{L}^{-1}$ P25-0.70%Pt).

Keywords: carbon dioxide; photocatalysis; photoreduction; methane; methylene blue



Academic Editor: Wanhong Ma

Received: 14 August 2025 Revised: 11 September 2025 Accepted: 17 September 2025 Published: 28 September 2025

Citation: Pulido-Melián, E.; Santana-Fleitas, C.V.; Araña, J.; González-Díaz, Ó.M. Simultaneous Photocatalytic CO₂ Reduction and Methylene Blue Degradation over TiO₂@(Pt, Au, or Pd). *Photochem* **2025**, 5, 30. https://doi.org/10.3390/ photochem5040030

Copyright: © 2025 by the authors. Licensee MDPI, Basel, Switzerland. This article is an open access article distributed under the terms and conditions of the Creative Commons Attribution (CC BY) license (https://creativecommons.org/licenses/by/4.0/).

1. Introduction

 CO_2 is the most important of the greenhouse gases, and its emissions continue to be a major concern. CO_2 is captured through separation processes, primarily through absorption or adsorption, and is subsequently stored [1]. However, ideally, it should be used as a raw material for conversion into other materials [2]. In the search for alternative energy sources and the reduction in greenhouse gas concentrations, the photocatalytic reduction of CO_2 has attracted attention since the oil crisis of the 1970s as it can lead to CO and other value-added compounds such as methane, methanol, or formic acid (Equations (1)–(5)).

$$CO_2 + 2e^- + 2H^+ \to CO + H_2O$$
 (1)

$$CO_2 + 2e^- + 2H^+ \to HCO_2H$$
 (2)

$$CO_2 + 4e^- + 4H^+ \to CH_2O + H_2O$$
 (3)

$$CO_2 + 6e^- + 6H^+ \to CH_3OH + H_2O$$
 (4)

$$CO_2 + 8e^- + 8H^+ \to CH_4 + 2H_2O$$
 (5)

Photochem **2025**, 5, 30 2 of 18

The photocatalytic reduction of CO_2 occurs under relatively mild conditions and with low energy consumption, as, unlike thermal reduction, it does not require reaching demanding pressure and/or temperature conditions. The first works on the photocatalytic reduction of CO_2 in aqueous solution were published between 1978 and 1979 [3,4]. Both of these publications were photoelectrochemical-based works, which, although presenting advantages over heterogeneous photocatalysis in terms of controllability and selectivity, face greater problems in terms of the stability of the materials [5].

In recent years, the focus of much of the research conducted has been on the construction and modification of catalysts to improve their activity and selectivity [6–9]. Catalysts need to be stable against corrosion, harmless, low-cost, and have suitable physicochemical characteristics, namely a broad bandgap that provides adequate positive and negative redox potentials in the valence and conductance bands, respectively. Although many materials have been and continue to be explored, TiO_2 remains the material that best meets this requirement [10].

One of the reasons for the decreasing efficiency of the photocatalytic process is that the photogenerated electrons and holes recombine before reaching the surface of the semiconductor. In order to decrease the recombination rate, metallic nanoparticles that concentrate the generated photoelectrons that go to the conduction band are incorporated. Zhang et al. photodeposited Pt nanoparticles on TiO_2 nanoparticles and nanotubes and found the optimal Pt percentage to be 0.12 wt% for the production of CH₄ [11]. In a more recent work, Nabil et al. also deposited Pt on TiO_2 and a composite of it with reduced graphene oxide (rGO), obtaining CH₃OH as the major product and demonstrating that photocatalysis showed better activity in CO_2 reduction than photoelectrochemistry [12]. In their work, Pougin et al. explored the benefit of Au particles through a combination with core–shell type TiO_2 and obtained as main products CH_4 (5 μ mol·g⁻¹·h⁻¹) and CO [13]. Yu et al. published how it is possible to use only Au nanoparticles as a catalyst to produce the photoreduction of CO_2 under visible light and in the presence of water [14]. Su et al. compared Pt, Au, and Pd on TiO_2 nanowire and obtained the maximum production of 26.74 μ mol·g⁻¹ of CH₄ and 50.43 μ mol·g⁻¹ of CO with 0.5% of Pd [15].

It is also important to employ substances that take advantage of the photogenerated holes in the valence band of the semiconductor to prevent recombination. In general, water acts as an electron donor but presents drawbacks such as the formation of oxygen and protons that compete with the reduction of CO_2 (Equation (6)). Therefore, water may be added or, indeed, other substances known as sacrificial agents that do not present these drawbacks [16] and can even increase the solubility of the CO_2 in the liquid phase [17].

$$2H_2O + 4h^+ \rightarrow O_2 + 4H^+$$
 (6)

Both inorganic and organic substances have been used as sacrificial agents, with the former including aqueous solutions based on bicarbonates, carbonates, hydroxides, or sulfites. Yoshino et al., with $\text{CoO}_x/\text{BiVO}_4@\text{rGO}@(\text{CuGa})_{0.5}\text{ZnSe}$ and employing different base additives as sacrificial agents (SO_3^{2-} , HCO_3^- , NaOH), obtained H_2 and CO as the major products [18], while Yang et al., with Cu-TiO_2 and Pt-TiO $_2$ and a solution of sodium carbonate and sodium sulfate at pH 3, obtained H_2 and CH_4 in the gaseous phase and detected HCOOH, HCHO and CH $_3$ OH in liquid phase [19].

With respect to organic sacrificial agents, use has principally been made of alcohols such as isopropanol or ethanol and amines such as triethanolamine or triethylamine [20–24]. However, the use of organic sacrificial agents and/or solvents is controversial as they may not be sufficiently stable and, as a result of their decomposition, the reaction products of CO₂ reduction may be overestimated [25,26]. It has recently been discovered that the role of these substances could be more complex than simply acting as a hole-trapping agent.

Photochem **2025**, 5, 30 3 of 18

For example, triethanolamine (TEOA), which has been widely used as a sacrificial agent, appears to not only act as a hole-trapping agent but is also capable of photocatalyzing the reduction of CO₂ to CH₄ and CO under UV radiation [27].

The proposal has recently been made to simultaneously carry out the oxidation of a contaminant with the photoreduction of CO₂. Liu et al. synthesized oxygen-doped carbon nitride nanotubes with which they obtained CO from CO₂ reduction and lactic acid from xylose oxidation [28].

In the context described above, this work aims to use an aqueous solution of methylene blue (MB), a toxic and non-biodegradable cationic dye, as an electron donor. The extensive use of MB in various applications (including textiles, medical, pharmaceuticals, biological staining, and chemicals) generates a significant volume of waste that needs to be treated [29–31]. It is also considered the model molecule for various applications. It is employed to study the adsorption capacity of activated carbons and, since it practically does not absorb in the UVA range, it has been used as a target substance to test the activity of photocatalysts under aerated conditions with UVA radiation, as under these conditions it does not undergo transformation by photosensitization or, in practical terms, by photolysis [32]. In a recent study by Lee et al., its use was suggested to test catalysts under anaerobic conditions in both UVA and Vis [33].

The novelty of the work presented here lies in the fact that, to our knowledge, no studies have proposed the simultaneous removal of the MB contaminant with the reduction of CO_2 through heterogeneous photocatalysis, nor has any publication contemplated the mineralization of MB under anaerobic conditions. This work therefore studies the removal and use of MB as a sacrificial agent for CO_2 reduction using TiO_2 -based catalysts (P25 and P90 from Evonik), modified with metal deposits, and examining variables such as pH, catalyst load, metal load, and MB concentration.

2. Materials and Methods

2.1. Materials

Methylene blue trihydrate ($C_{16}H_{18}ClN_3S\cdot 3H_2O$) was supplied by Sigma-Aldrich (Darmstadt, Germany). All solutions were made with deionized water (MilliQ). For pH adjustment, sodium hydroxide and hydrochloric acid solutions were used. The catalysts were the TiO₂ Aeroxide P25 (P25) and TiO₂ Aeroxide P90 (P90) from Evonik (Essen, Germany) (Table 1). The precursors of the metals deposited on the catalysts were hexachloroplatinic (IV) acid hexahydrate ($H_2PtCl_6\cdot (H_2O)_6$) for platinum (Pt), tetrachloroauric (III) acid trihydrate ($HAuCl_4\cdot (H_2O)_3$) for gold (Au), and palladium (II) nitrate ($PdNO_3\cdot (H_2O)_2$) dihydrate for palladium (Pd).

Catalyst	Anatase/%	Rutile/%	Crysta	l Size	Surface	Dan daan /aW	Pore Volume/cm ³ ·g ⁻¹	
			Anatase/nm	Rutile/nm	Area/m ² ·g ⁻¹	Bandgap/eV		
P25	82	18	23	44	48.6 ± 0.1	3.18	0.176	
P90	86	14	13	19	79.2 ± 0.2	3.27	0.381	

Note: Data taken from [34].

2.2. Methods

2.2.1. Metal Deposition

The amounts of metals loaded were 0.35 ± 0.03 and 0.70 ± 0.05 wt% with respect to the mass of the catalyst. The photocatalysts obtained were named P25-x%M and P90-x%M, where x denotes the metal mass percentage and M corresponds to Pt, Au, or Pd, as applicable. The method employed for metal deposition has been previously

Photochem **2025**, 5, 30 4 of 18

described [35–37]. In an immersed reactor (Photochemical Reactors Ltd., Sonning Common, UK) with stirring, 2 g of photocatalyst were dispersed into 400 mL of deionized water and 9.2 mL of isopropanol and subjected to magnetic stirring. The dissolved oxygen was removed from the solution with a nitrogen flow bubbling that was maintained for the whole process. After 30 min, the required amount of metal was added from a concentrated solution of the precursor and then irradiated with a 400 W medium-pressure Hg lamp $(8.1 \times 10^{-7} \, \text{einstein s}^{-1} \cdot \text{L}^{-1})$ placed inside a quartz tube for 4 h. The catalyst was separated and washed with water 3 times by centrifugation. Finally, it was dried at 105 °C for 24 h and ground in an agate mortar.

2.2.2. Activity Tests

In a borosilicate glass reactor, 75 mL of MB solution was added, and the required amount of catalyst was incorporated. The pH was adjusted, and the reactor was incorporated into the test setup (Figure 1). The reactor was continuously stirred, and the air purged from the system by circulating He for 30 min at 150 mL·min $^{-1}$. Subsequently, three Philips HB175 Solarium lamps were turned on, each equipped with four 15 W Philips CLEO fluorescent tubes with a maximum radiation at 365 nm. The lighting was maintained for 24 h. The gases generated in the reactor were directed to a MicroGC (490 Agilent Technologies, Santa Clara, CA, USA) through a total flow of 5 mL·min $^{-1}$ of He (4.5 mL·min $^{-1}$) and CO₂ (0.5 mL·min $^{-1}$). The chromatographic areas were converted to molar flows by performing calibration curves. The MicroGC uses He as a carrier gas and is equipped with two columns, a MolSieve5A and a PoraPLOT Q column, and a thermal conductivity detector.

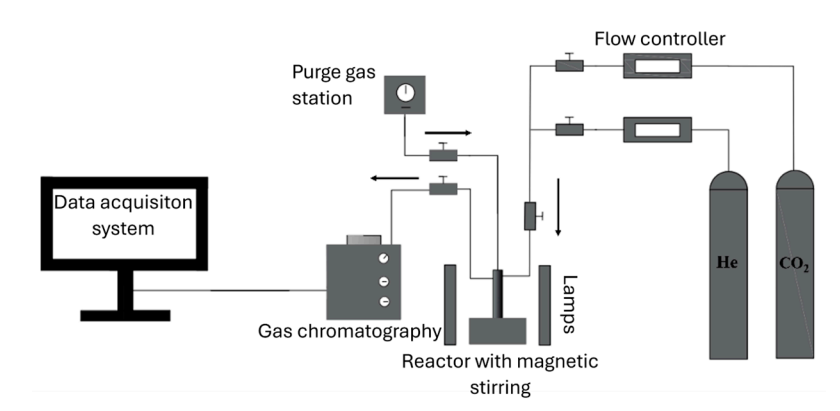


Figure 1. Schematic representation of the reaction system.

At the end of the experiment, the liquid was separated from the solid by centrifugation and 0.45 μ m filtration, and both parts were subjected to further analysis. The solid part was studied using Fourier transform infrared spectroscopy (FTIR). For this purpose, a Nicolet iS10 device from Thermo Fisher Scientific (Waltham, MA, USA) was used. The samples were analyzed in transmission mode, placed between CaF₂ windows. The spectra were recorded in the range of 4000–1000 cm⁻¹ with a resolution of 4 cm⁻¹ and 32 scans. The liquid part was analyzed by UV/Vis spectroscopy (Libra S60, Biochrom, Cambridge, UK), high-resolution liquid chromatography (1200 Infinity Agilent Technologies), and gas chromatography (2010 Plus Shimadzu Europe GmbH, Duisburg, Germany), and the organic and inorganic carbon was quantified (Shimadzu TOC-VCSN). The amount of residual MB was quantified with UV/Vis spectroscopy. The presence of carboxylic acids was analyzed by liquid chromatography, using a Supelcogel C610-H column, with a mobile phase of 0.1% phosphoric acid in water at a flow rate of 0.5 mL·min⁻¹ and a UV/Vis detector at 210 nm. Gas chromatography was employed to analyze the presence of highly volatile alcohols,

Photochem **2025**, 5, 30 5 of 18

aldehydes, or ketones of low molecular weight, for which a CP-Wax 52 CB 30 m \times 0.25 mm \times 0.5 μ m (Agilent) column and a flame ionization detector (FID) were used.

3. Results and Discussion

Activity tests were conducted with unmodified P25, with no signals detected in the gas phase despite a 92.3% degradation of MB and a 76.4% mineralization under the conditions of 20 ppm MB with 2 g·L $^{-1}$ P25 and pH 5. With the aim of obtaining an active catalyst for both processes, CO₂ reduction and MB removal, metal photodeposition was carried out on the surface of the P25 catalyst, which is the reference TiO₂-based catalyst in photocatalytic studies [38–40]. The variables of pH, catalyst load, metal deposit load, and sacrificial agent concentration were analyzed with the P25, the results of which are discussed below. Subsequently, the previous optimal conditions were tested with P90, which is a catalyst from the same commercial house with slight modifications in its characteristics (see Table 1). Further comments on the P90 catalyst can be found in Section 3.6.

3.1. Effect of pH

Figure 2 shows the graphs of the evolution of the molar flows of methane and hydrogen for different pH values. The pHs measured at the end of the experiment were practically the same as the initial ones for pH 3 and pH 5, with an increase and decrease, respectively, of less than 0.2 units. For pH 7, there is a slightly greater decrease of 0.6 units. However, for pH 9, the decrease is 3.4 units.

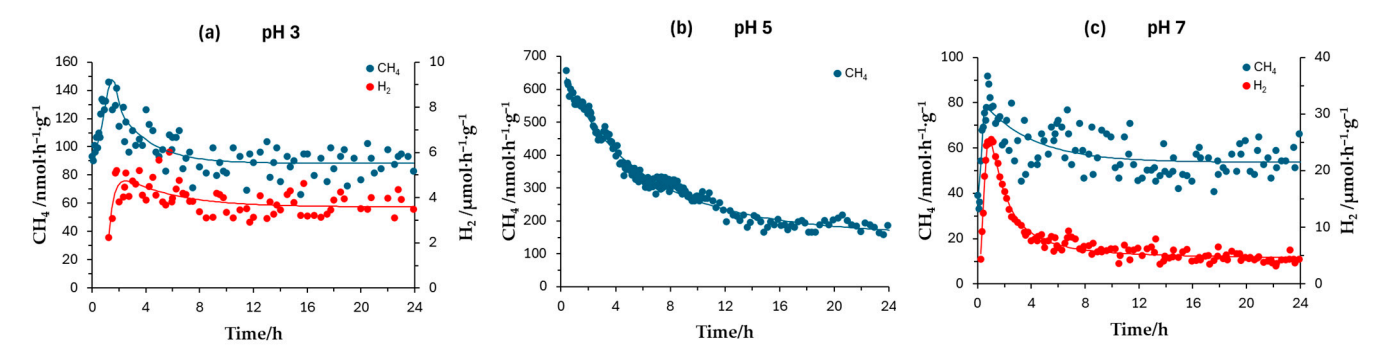


Figure 2. Evolution of methane and hydrogen in the case of the P25-0.35%Pt at different pHs: (a) pH 3, (b) pH 5, and (c) pH 7 (20 ppm MB, 2 g·L $^{-1}$ P25-0.35%Pt).

For pH 3, both CH₄ and H₂ were obtained in the gas phase. The CH₄ shows an initial increase in flow up to 150 nmol·h⁻¹·g⁻¹ and then decreases to remain constant in a range of 80–100 nmol·h⁻¹·g⁻¹. In the case of the H₂, a very inconsistent flow over time is observed, with values around 3.5 µmol·h⁻¹·g⁻¹. For pH 5, only CH₄ was obtained. Initially, a flow of 700 nmol·h⁻¹·g⁻¹ was achieved, which then decreased and stabilized around 200 nmol·h⁻¹·g⁻¹. In the case of pH 7, the results show the presence of H₂ and CH₄. The H₂ increases over the first 30 min, reaching a flow above 25 µmol·h⁻¹·g⁻¹, and then decreases, stabilizing at around 5.00 µmol·h⁻¹·g⁻¹. The CH₄, which reaches a maximum of 90 nmol·h⁻¹·g⁻¹, remains practically constant at around 60 nmol·h⁻¹·g⁻¹.

In short, at pH 3, both H_2 and CH_4 are produced, at pH 5, the production of CH_4 is favored and is significantly higher than that obtained at the other tested pH levels, and at pH 7, the production of CH_4 is drastically reduced while the production of hydrogen is greatly increased compared to that obtained at pH 3 and pH 5. At pH 9, no methane or hydrogen production was observed.

The adsorption of MB on TiO_2 is low [41–43]. Zeng et al. determined a maximum adsorption of $5.5 \cdot 10^{-7}$ mol·g⁻¹ at pH 5 [42]. Figure 3a shows the infrared spectrum of the P25-0.35%Pt with MB at CH₄ at different concentrations. The band at 3400 cm⁻¹

Photochem **2025**, 5, 30 6 of 18

corresponding to the OH groups (not shown) and the band at 1635 cm⁻¹ corresponding to water are not shifted as a result of the presence of MB. In the 2000–1000 cm⁻¹ region, various bands of the MB can be observed which are visible when it is adsorbed on the P25-0.35%Pt [44,45]: the band at 1603 cm⁻¹ corresponding to the skeletal stretching vibrations of the C=C and C=N bonds in the heterocycle, the band at 1490 cm⁻¹ assigned to the C=S stretching vibration, the band at 1393 cm⁻¹ assigned to C-H bending vibrations, the peaks at 1336 cm⁻¹ and 1357 cm⁻¹ corresponding to the C-N and C=S⁺ stretching vibrations of the heterocycle, the band at 1252 cm⁻¹ of the in-plane and out-of-plane bending of the C-H bonds, another band at 1223 cm⁻¹, which corresponds to the stretching vibration of the C-C bonds of the heterocycles, and those at 1178 cm⁻¹ and 1143 cm⁻¹ corresponding to the in-plane bending vibrations of the C-H and C-N bonds, respectively, of the heterocycles. The band at 1603 cm⁻¹ presents a notable shift with respect to the MB band at 1595 cm⁻¹. Smaller shifts are observed for the bands at 1393 cm⁻¹, 1336 cm⁻¹, and 1143 cm⁻¹. This could indicate that the adsorption of MB molecules on the surface of the P25-0.15%Pt is preferably planarly adsorbed towards the TiO₂ surface [46].

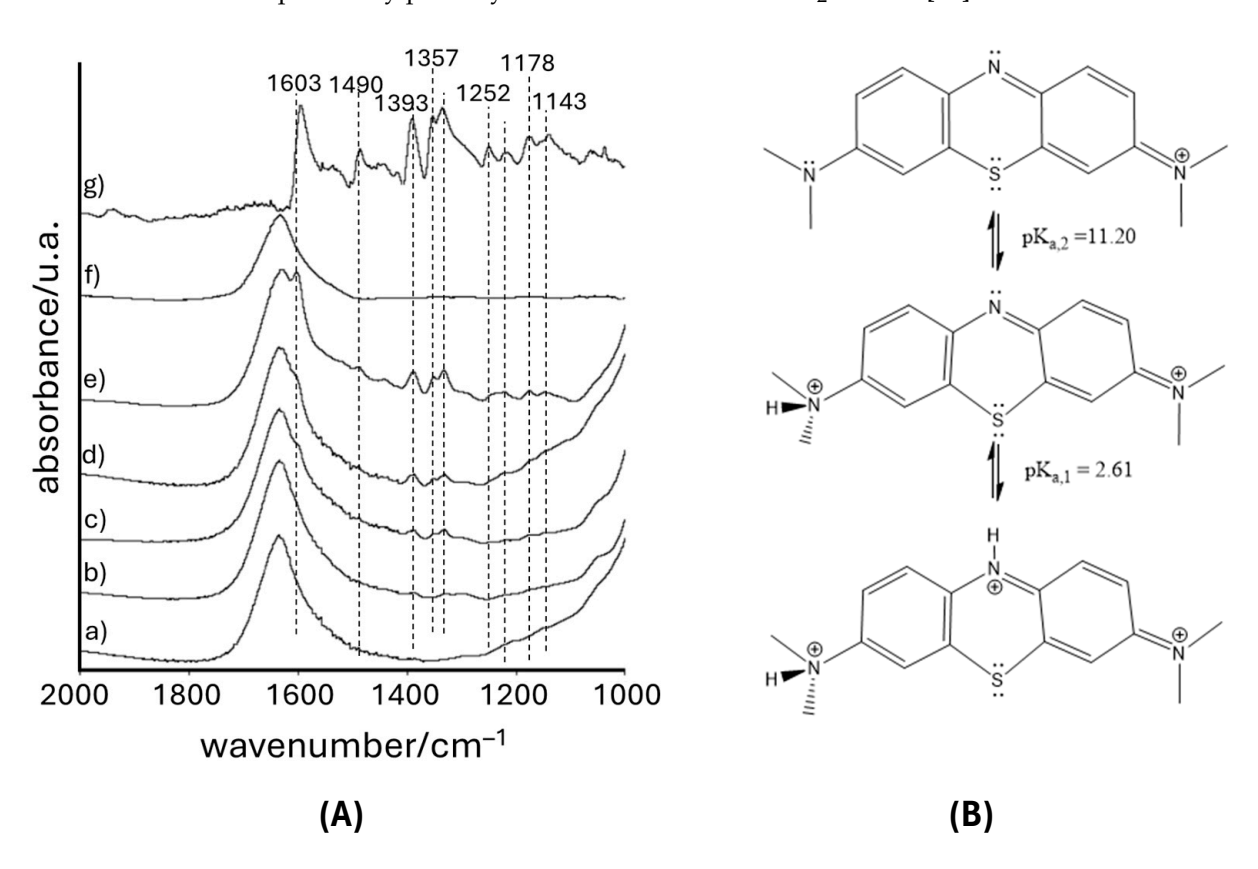


Figure 3. (**A**) FTIR spectra of P25-0.35%Pt with MB adsorbed at pH 5 at different concentrations: (a) 20 ppm, (b) 60 ppm, (c) 100 ppm, (d) 250 ppm, (e) 500 ppm, (f) P25-0.35%Pt, and (g) MB. (**B**) Dissociation of MB in water as a function of pH.

Adsorption is conditioned by pH. The zero charge point (pH_{ZC}) of the P25-0.35%Pt is around 6.8. For its part, the MB has two pKa, 2.63 and 11.20 [47], which is why it is a cationic dye across the entire pH range. Thus, below pH 2, the molecule presents three positive charges, at pH 4–10, two positive charges, and, finally, above 12, only one positive charge (Figure 3b). Figure S1 (Supplementary Materials) shows the adsorption spectra of the MB on P25-0.35%Pt at different pH levels. It can be seen that the bands are much more intense at pH 7, 9, and 12 than at pH 3 and pH 5. At pH 3, the surface of the highly positively charged catalyst repels the adsorption of MB, which has two and three positive charges. At pH 5, although to a lesser extent, the surface of P25 still presents a positive charge, and

Photochem **2025**, 5, 30 7 of 18

the MB molecule has two positive charges, which continues to pose an impediment to adsorption, although not as severe as at pH 3.

The dissolution of CO_2 in water produces the formation of carbonic acid, as well as bicarbonate and carbonate anions, whose proportion and predominance will depend on the pH of the medium. Therefore, the supply of CO_2 gas generates the formation of negatively charged species that could cause a partial neutralization of the divalent cationic species, MBH^{2+} , facilitating the approach to the surface of the photocatalyst through ionic interaction due to the formation of a bicarbonate-MB binding [48]. Carbonic acid has two pKa values, 6.3 and 10.3. This means that at pH 5, there is a greater amount of bicarbonate ions (HCO_3^-) than at pH 3, which increases the likelihood of this effect occurring. However, at pH 3, carbonic acid overwhelmingly predominates. Therefore, it is proposed that bicarbonate ions help neutralize and attract the MBH_2^+ towards the surface of the photocatalyst, acting as an aid for the anoxic degradation of MB directly or indirectly through the action of hydroxyl radicals generated by water oxidation [49,50]. This could help explain the improvement in methane production when moving from pH 3 to pH 5 and the deterioration in H_2 , which at pH 3, is benefited by the higher presence of H^+ in solution.

The most advantageous situation for the adsorption of the MB, which still carries two positive charges, should, in principle, be at pH 7, when the TiO_2 surface would have a practically neutral charge. However, at this pH, there is a significant accumulation of anions, especially bicarbonates (almost 83% relative to the CO_2 saturation value). In fact, inorganic carbon was measured at 6.16 ppm compared to values below 1 ppm obtained for pH 3 and pH 5. This excess could, on the one hand, be competing with the MB for the adsorption sites [51] and, in addition, be favoring alternative and slower mechanisms for MB oxidation through the formation of $CO_3^{\bullet-}$, which hinders methane formation [52,53]. In fact, MB degradation values of 99.7% and 99.8% were achieved at pH 3 and 5, respectively, while at pH 7, the value was slightly lower, at 98.4%. These values are as high as those obtained under more advantageous conditions with the presence of air [54,55]. The amount of residual total organic carbon was 4.1, 4.5, and 4.9 ppm for pH 3, pH 5, and pH 7, respectively.

With the aim of seeing the effect of the CO_2 on the activity, the experiment at pH 5 was repeated, replacing CO_2 with He. It can be seen in Figure 4A that only hydrogen is produced without CO_2 , showing that the methane formed comes from reduction in the CO_2 supplied to the reaction medium [23,56]. The CO_2 acts as an electron acceptor on the surface of the photocatalyst, initiating its reduction to products such as CH_4 . On the other hand, the absence of CO_2 favored the appearance and production of hydrogen [57]. This is because it reduces the competition for capturing the photogenerated electrons, and the only alternative reactions are the reduction of protons and the MB. In the FTIR spectra at the end of the test, bands at 1689 cm^{-1} , 1550 cm^{-1} , 1511 cm^{-1} , 1398 cm^{-1} , and 1060 cm^{-1} are only observed in the presence of CO_2 , demonstrating the formation of adsorbed CO_2 species and essential intermediate species resulting from its reduction (Figure 4B) [58–61]. The MB, however, does degrade, leaving only 0.10 ppm in solution and a total organic carbon amount of 5.4 ppm, values which are only slightly higher than those observed in the presence of CO_2 .

Photochem **2025**, 5, 30 8 of 18

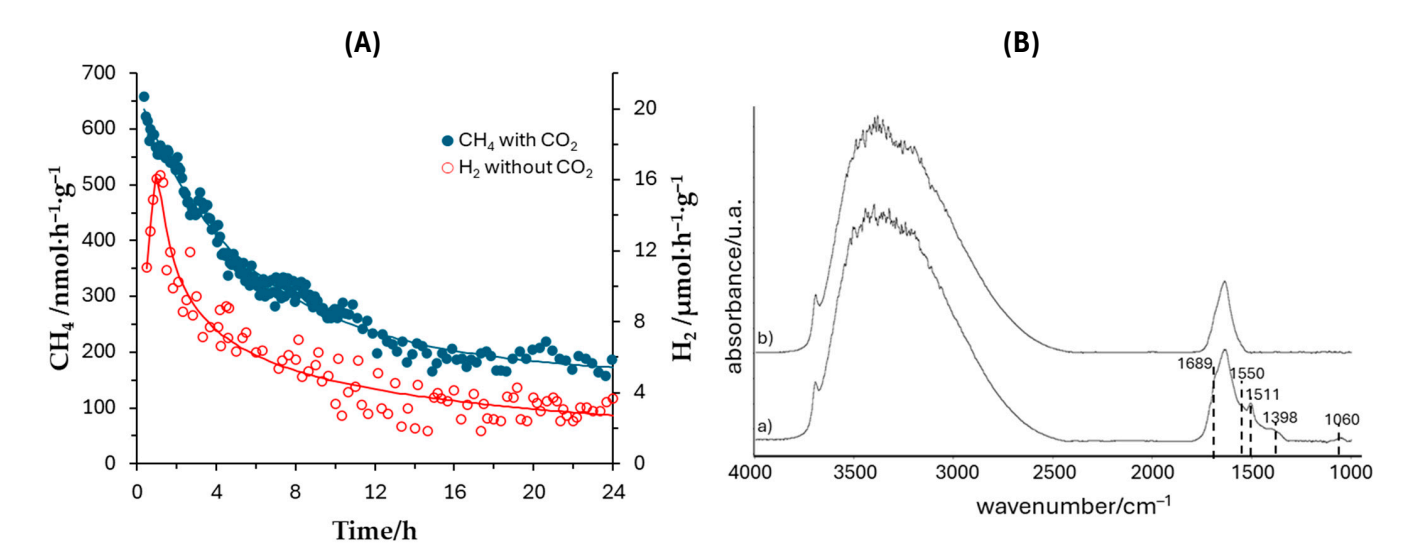


Figure 4. (A) Evolution of the molar flows of methane and hydrogen with and without CO_2 , and (B) FTIR spectra after 24 h of illumination with (a) and without (b) CO_2 flow (20 ppm MB, pH 5, 2 g·L⁻¹ P25-0.35%Pt).

3.2. Effect of Catalyst Load

In order to try to increase methane production, the catalyst load was increased. In Figure 5, a comparison is made between $2 \text{ g} \cdot \text{L}^{-1}$ and $4 \text{ g} \cdot \text{L}^{-1}$.

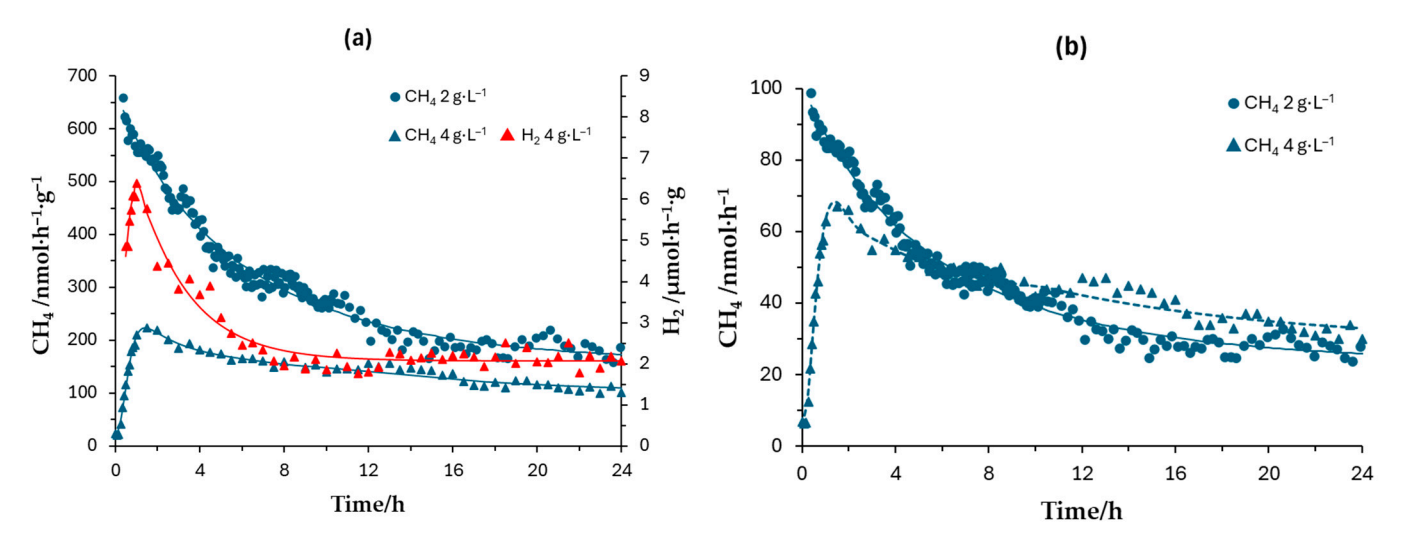


Figure 5. (a) Evolution of molar flows per unit mass of catalyst; and (b) evolution of total molar flows for $2 \text{ g} \cdot \text{L}^{-1}$ and $4 \text{ g} \cdot \text{L}^{-1}$ P25-0.35%Pt (20 ppm MB, pH 5).

With respect to CH₄ production, for 2 g·L⁻¹, the production almost immediately reaches a value of around 658 nmol·h⁻¹·g⁻¹ and decreases to 158 nmol·h⁻¹·g⁻¹. In contrast, an induction period is observed for a catalyst load of 4 g·L⁻¹, with a maximum flow of 223 nmol·h⁻¹·g⁻¹ subsequently reached, which decreases more slowly over 24 h to 103 nmol·h⁻¹·g⁻¹ (Figure 5a). These lower flows per unit mass for 4 g·L⁻¹ highlight the adverse effects of catalyst aggregation and radiation scattering [62–64]. In fact, when integrating the total production over 24 h, very similar values are obtained for 2 and 4 g·L⁻¹, namely 1033 and 1047 nmol, respectively (Figure 5b).

A notable difference between the two experiments is that H_2 was produced in addition to CH_4 with the increase in the amount of catalyst, increasing in the first hour to $6.4~\mu\text{mol}\cdot\text{h}^{-1}\cdot\text{g}^{-1}$ and then stabilizing at around $2.0~\mu\text{mol}\cdot\text{h}^{-1}\cdot\text{g}^{-1}$ after 7 h. This may be

Photochem **2025**, 5, 30 9 of 18

due to the greater number of active sites and poor diffusion of the CO₂ in the reactor, which reduces its ability to compete with water/protons for the photogenerated electrons [65].

The effect of catalyst load is also reflected in the degradation of the MB, which was completely removed, with a higher mineralization degree, increasing from 62% for $2 \text{ g} \cdot \text{L}^{-1}$ to 91% for $4 \text{ g} \cdot \text{L}^{-1}$.

3.3. Effect of Platinum Load

The aim in this section is to study the effect of the amount of platinum, a metal that produces a beneficial effect in small percentages [66]. For this purpose, two quantities were compared, 0.35% and 0.70%, by weight relative to the mass of TiO₂ (Figure 6).

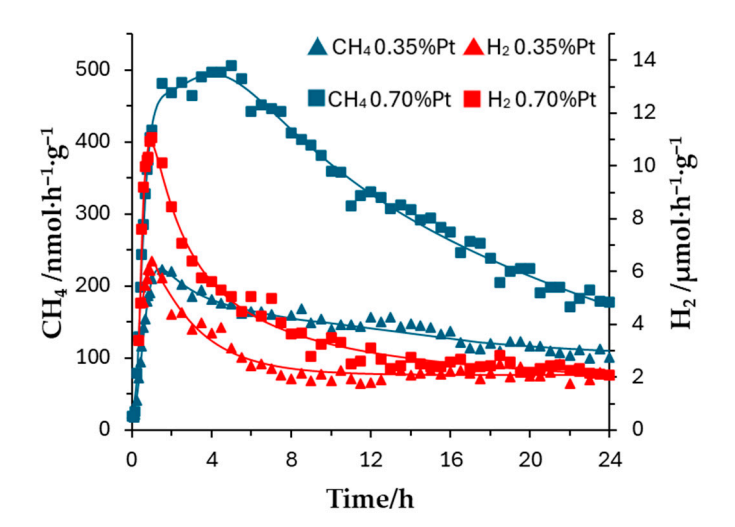


Figure 6. Evolution of the molar flows of methane and hydrogen as a function of platinum loading (20 ppm MB, pH 5, 4 g·L $^{-1}$ P25-x%Pt).

For the lower platinum load, as previously observed, the CH₄ reaches a maximum flow of 220 nmol·h⁻¹·g⁻¹ in 1.5 h and then decreases to stabilize at around 100 nmol·h⁻¹·g⁻¹, while the H₂ reaches a maximum of 6.8 μ mol·h⁻¹·g⁻¹ in the first hour and then falls to stabilize at around 2 μ mol·h⁻¹·g⁻¹.

With respect to the higher platinum load, the CH_4 increases to a maximum of 500 nmol·h⁻¹·g⁻¹ in 5 h and decreases to stabilize at around 200 nmol·h⁻¹·g⁻¹. The H_2 flow gradually increases before reaching a maximum value of 11 μ mol·h⁻¹·g⁻¹ in 1 h, and then decreases, initially more rapidly and then after 10 h more slowly, to 2 μ mol·h⁻¹·g⁻¹.

Comparing both experiments, the amount of H_2 and CH_4 produced in 24 h with the P25-0.70–Pt catalyst is greater than with the 0.35% Pt catalyst: for CH_4 , 7.88 μ mol·g⁻¹ vs. 1.04 μ mol·g⁻¹, and for H_2 , 89.67 μ mol·g⁻¹ vs. 61.03 μ mol·g⁻¹. Observing the results, it is concluded that a higher density of metallic active sites favors charge separation and, therefore, improves the overall efficiency of the photocatalytic process. Moreover, it is observed that, although the reduction in H^+ and H_2O to produce H_2 continues to be important, the CH_4 : H_2 ratio increases with the amount of Pt.

Regarding MB degradation, it is observed that the remaining MB concentration is below 0.05 ppm in both cases, but that a higher amount of Pt resulted in a decrease in mineralization, leaving 3.3 ppm (28%) of total organic carbon. It has been reported in the literature that the presence of metal deposits does not always favor the oxidation of organic contaminants [67].

3.4. Effect of Methylene Blue (MB) Concentration

Figure 7 shows the molar flows of methane and hydrogen produced for 10, 20, 50, and 100 ppm of MB. An experiment was also conducted in the absence of MB, but only a

continuous hydrogen signal was detected from the first hour, which could not be quantified (<1.4 μ mol·h⁻¹·g⁻¹). This highlights the fundamental role of MB as a sacrificial agent for CO₂ reduction.

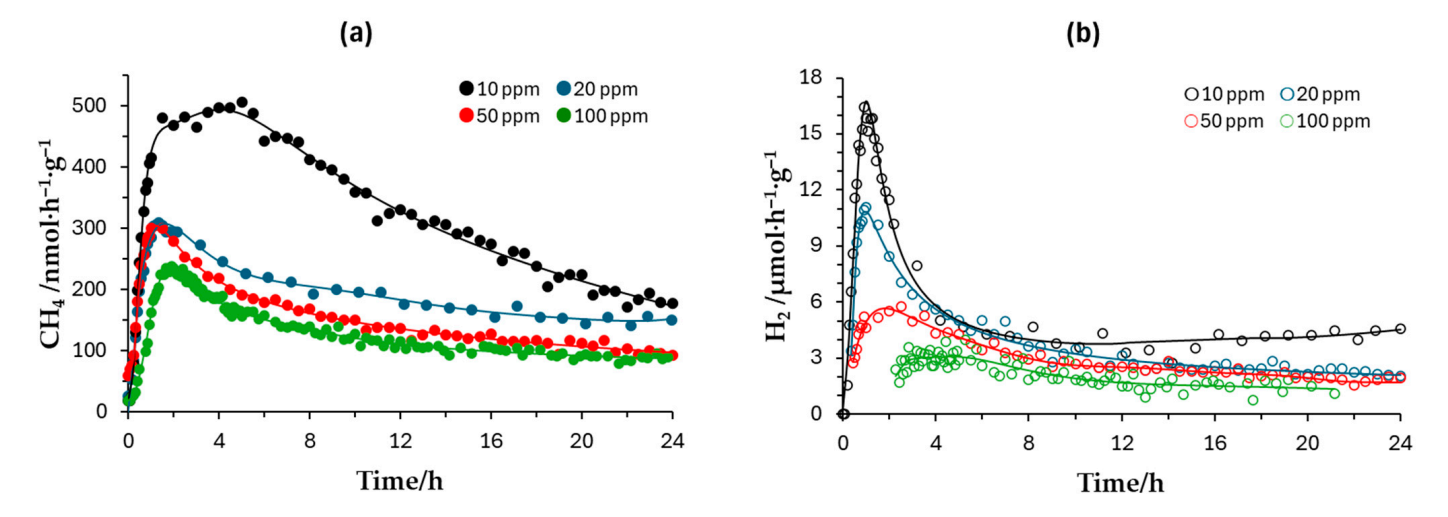


Figure 7. Evolution of the molar flows of (a) methane and (b) hydrogen as a function of methylene blue concentration (pH 5, 4 g·L $^{-1}$ P25-0.70%Pt).

With the increase from 10 to 20 ppm of MB, an increase in methane flow is observed. For 10 ppm of MB, a maximum of 310 nmol·h⁻¹·g⁻¹ is reached at 1.3 h, and from there it gradually decreases to about 23 nmol·h⁻¹·g⁻¹ at 24 h, which is a value only slightly lower than the value reached for the case of 20 ppm at this time. However, for 20 ppm, a maximum of 500 nmol·h⁻¹·g⁻¹ is reached, so its decline is faster. In the case of hydrogen, the opposite happens, and the maximum reached at 10 ppm is higher, 16 µmol·h⁻¹·g⁻¹ vs. 11 µmol·h⁻¹·g⁻¹. At concentrations above 20 ppm, both the methane and hydrogen flows decrease. For 50 ppm, a maximum of CH₄ of 301 nmol·h⁻¹·g⁻¹ is reached, and for 100 ppm, 238 nmol·h⁻¹·g⁻¹, and in both cases, decreasing to 96 nmol·h⁻¹·g⁻¹ at 24 h. The H₂ for 50 ppm appears after 30 min of illumination, reaching a maximum of 57 µmol·h⁻¹·g⁻¹ at 2.5 h and then falling to 1.9 µmol·h⁻¹·g⁻¹ at 24 h, while for 100 ppm of MB, it is quantifiable after 2.25 h with flows of between 1 and 1.5 µmol·h⁻¹·g⁻¹.

The optimal sacrificial agent concentration was 20 ppm. The reduction in activity with the increase in sacrificial agent concentration can be attributed to the saturation of active sites and the formation of a contaminant layer on the surface, which acts as a physical and electrostatic barrier, hindering the interaction between CO₂ and water and the catalytic centers. Therefore, in aqueous systems, it is important to optimize the concentration of the sacrificial agent to increase efficiency [23].

As can be seen in Table 2, the concentration of MB and total carbon remaining in solution after 24 h is higher the greater the initial concentration of MB. This is consistent with the detection, for 100 ppm of MB, of a higher concentration of intermediates such as phenol and ethanol compared to carboxylic acids, which are intermediates in the later stages of degradation and which are observed for lower MB concentrations [54,68,69]. In any case, the mineralization achieved for 100 ppm of MB is high, at 80.5%.

Catalyst/[MB] _o /Metal	[MB]	% MB _{degradated}	TOC	% TOC _{removed}	[Phenol]	[Ethanol]	[Formic Acid]	[Acetic Acid]	[Oxalic Acid]	[IC]
P25/10 ppm/Pt	ND	100	1.3	78.3	ND	ND	0.85	0.58	ND	0.3
P25/20 ppm/Pt	ND	100	3.3	72.5	0.01	ND	ND	ND	0.19	0.8
P25/50 ppm/Pt	0.3	99.0	9.2	69.3	0.07	ND	0.29	0.52	0.29	0.1
P25/100 ppm/Pt	1.5	97.5	11.7	80.5	0.08	5.6	0.18	ND	ND	0.1
P25/20 ppm/Au	0.3	97.5	6.1	49.2	0.04	ND	ND	ND	0.08	0.8
P25/20 ppm/Pd	ND	100	3.4	66.0	ND	ND	0.81	ND	1.1	0.9
P90/20 ppm/Pt	ND	100	1.2	90.0	0.04	ND	0.31	0.76	ND	4.8
P90/20 ppm/Au	ND	100	5.9	50.8	ND	ND	ND	0.40	ND	8.2

Table 2. Analysis in the liquid phase at 24 h of illumination (0.70% metal, pH 5, 4 g·L $^{-1}$).

Note: MB = methylene blue; ND = not detected; TOC = total organic carbon; and IC = inorganic carbon. The MB concentrations were estimated with a maximum of 664 nm. The concentrations are expressed in ppm of carbon.

3.5. Effect of the Nature of the Deposited Metal

In any study of heterogeneous photocatalysis, the role of noble metal deposits such as Ag, Au, Pd, and Pt on semiconductors in reducing the recombination of photogenerated charges is well known [70,71]. In the specific case of the photoreduction of CO_2 , its role in the selectivity or activation of the adsorbed CO_2 has also been considered [66,72–75]. Pt is one of the most studied of the aforementioned noble metals, with publications on its role in CO_2 adsorption dating back to the 1980s [76].

Figure 8a shows the flows of methane and hydrogen produced with the P25 modified with the different metals. In the case of Au, it is observed that methane increases to $180 \, \text{nmol} \cdot \text{h}^{-1} \cdot \text{g}^{-1}$ in the first $1.5 \, \text{h}$, then decreases and stabilizes at around $100 \, \text{nmol} \cdot \text{h}^{-1} \cdot \text{g}^{-1}$ after $7.5 \, \text{h}$. In this case, no hydrogen formation is observed, which can be related to previous studies that have shown that the optimal concentrations of Au for hydrogen formation are much higher than those of Pt and those considered in this study [36,37,77]. In the case of Pd, the methane reaches a maximum of $0.10 \, \mu \text{mol} \cdot \text{h}^{-1} \cdot \text{g}^{-1}$ at around $1.5 \, \text{h}$, then subsequently decreases and stabilizes at around $0.05 \, \mu \text{mol} \cdot \text{h}^{-1} \cdot \text{g}^{-1}$ after $8.5 \, \text{h}$. In this case, hydrogen formation is observed, reaching a maximum of $5.8 \, \mu \text{mol} \cdot \text{h}^{-1} \cdot \text{g}^{-1}$ at $1.5 \, \text{h}$ and stabilizing at around $2.0 \, \mu \text{mol} \cdot \text{h}^{-1} \cdot \text{g}^{-1}$ after $10.5 \, \text{h}$. These productions, of both methane and hydrogen, are lower than those obtained with Pt and previously discussed in earlier sections, where respective maximums of $500 \, \text{nmol} \cdot \text{h}^{-1} \cdot \text{g}^{-1}$ and $11 \, \mu \text{mol} \cdot \text{h}^{-1} \cdot \text{g}^{-1}$ were reached.

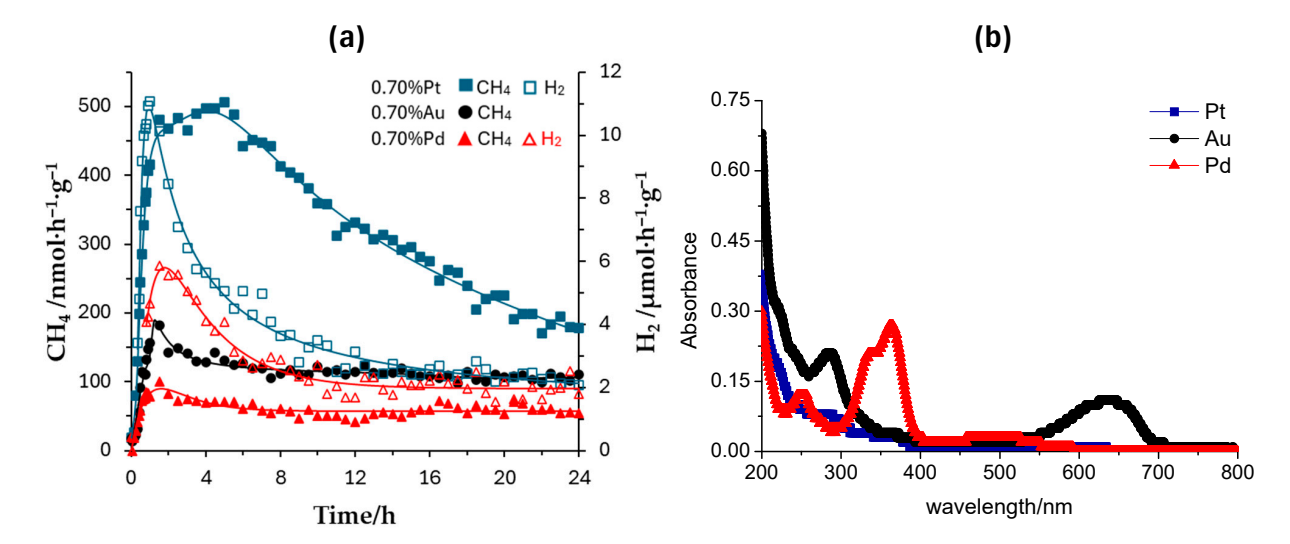


Figure 8. (a) Evolution of the molar flows of methane and hydrogen as a function of the nature of the metallic deposit (20 ppm MB, pH 5, 4 g·L $^{-1}$ P25-0.70%M). The CH₄ is represented by the filled-in symbols and the H₂ by the empty symbols. (b) UV-Vis spectrum at 24 h of illumination (20 ppm MB, pH 5, 4 g·L $^{-1}$ P25-0.70%M).

Ultimately, Pt was found to be the most effective for CH_4 production, followed by Au, while Pd showed the lowest efficiency. This comparison highlights the importance of the type of photodeposited metal in the optimization of TiO_2 -based photocatalytic catalysts for fuel generation applications. The fact that Pt is more efficient has been noted by other authors [66,78]. Khan et al. reported that Pt is the best metal due to its ease of dispersion on the surface of the TiO_2 -based photocatalyst and because it exhibits high activity for CO_2 hydrogenation [78].

As can be seen in Table 2, the case of Au is the only one where MB remains without being completely degraded, along with 50% of the total organic carbon. For Pd and Pt, the same levels of mineralization, 72%, are achieved. However, the degradation mechanism of MB with Pd is different because, despite the band in the UV/Vis spectrum at 664 nm disappearing, a band at 364 nm stands out, which was not observed as intensely in the other experiments, indicating a significant change at least in the kinetics of the MB degradation mechanism under anaerobic conditions (Figure 8b). In addition, when considering the FTIR spectra at the end of the tests (Figure 9), the catalyst with Pd shows much lower surface hydroxylation at this time compared to the catalysts with the other metal deposits. This is consistent with its lower methane production since hydroxylation seems to play a favorable role in CO_2 photoreduction [79–82].

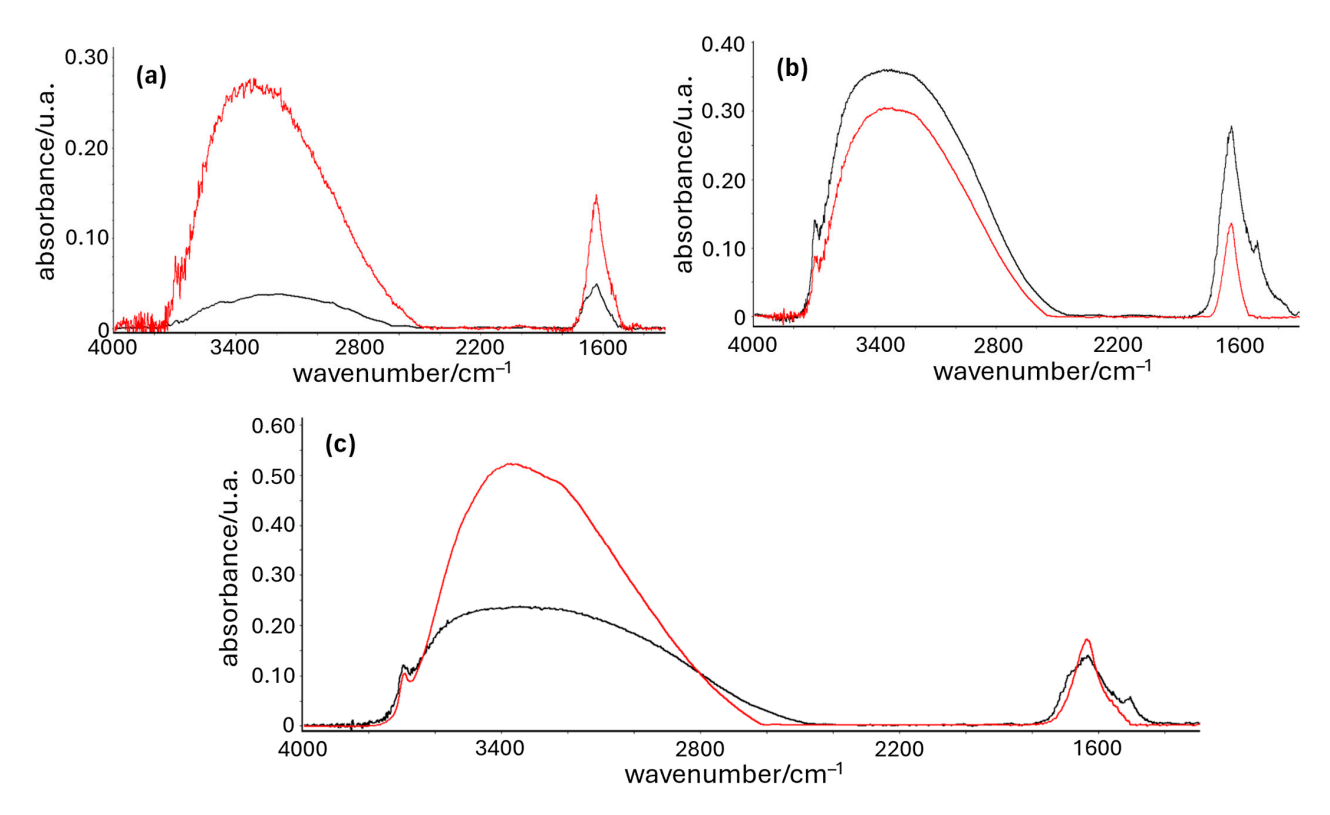


Figure 9. FTIR spectra of (a) P25-0.70%Pd, (b) P25-0.70%Au and (c) P25-0.70%Pt after 24 h of illumination (20 ppm MB, 4 g·L^{-1} P25-0.70%M, pH 5) (black line), and their reference spectra (red line).

3.6. TiO₂ Aeroxide P90

Like the P25, the P90 is a TiO_2 -based photocatalyst manufactured by Evonik. However, there are some key differences in their characteristics. The P25 has 82% anatase and the rest rutile, with crystal sizes of 23 nm and 44 nm, respectively, and a specific surface area of 48.6 m $^2 \cdot g^{-1}$. In contrast, the P90 has a higher percentage of anatase, 86%, with crystal sizes of 13 nm for anatase and 19 nm for rutile, which is smaller than in the case of P25. In addition, its specific surface area is somewhat higher at 79.2 m $^2 \cdot g^{-1}$ (Table 1) [34].

Although the P25 catalyst has historically been used and studied more in heterogeneous photocatalysis than the P90 catalyst, the latter has proven to be a competitive alternative, especially when looking for materials with a larger surface area or when used on supports or in mixtures with other photocatalysts [83–85]. However, it remains barely explored in the photoreduction of CO₂, with few references to its use found [60].

Figure 10 shows the results of three experiments conducted with the P90 catalyst in which the Pt load deposited on the surface and the catalyst load are varied. A fourth experiment was also conducted on another metal, Au.

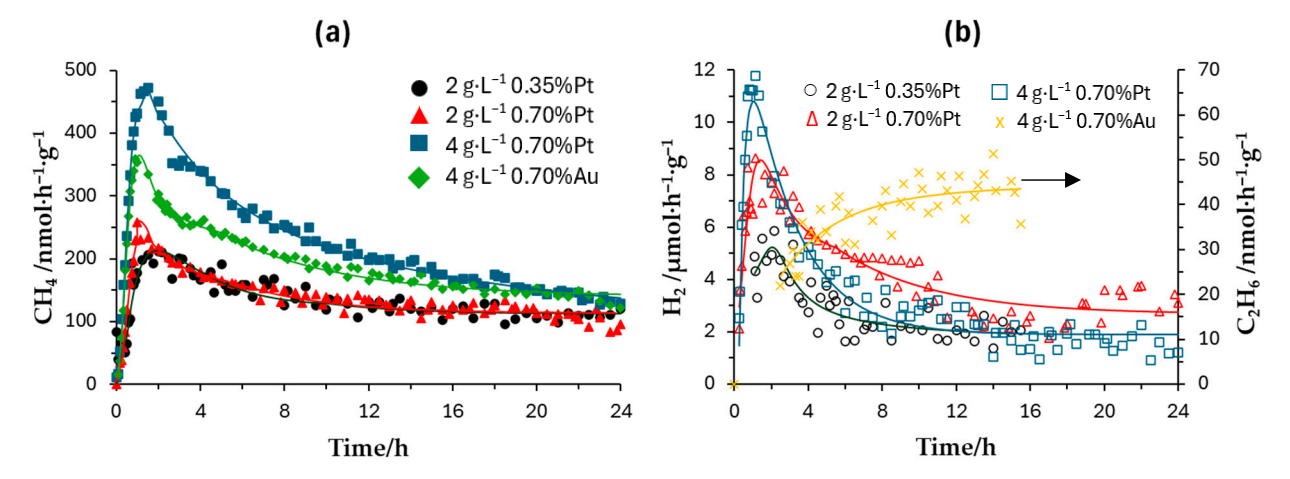


Figure 10. Evolution of the molar flows of (a) methane, and (b) hydrogen and ethane for tests conducted with the P90 catalyst (20 ppm MB, pH 5).

In the case of Pt, very low productions are obtained for $2 g \cdot L^{-1}$ of P90-0.35%Pt. It can also be seen that the CH₄ increases to 200 nmol·h⁻¹·g⁻¹ at 1.5 h and subsequently falls slowly to stabilize at 110 nmol·h⁻¹·g⁻¹ from 18.5 h. For its part, hydrogen appears between 1.1 h and 15.5 h with very low flows. This coincides with the case of the P25-0.35%Pt, where hydrogen was not observed under these same conditions.

When the amount of Pt deposition is increased, it is observed that the maximum methane flows increase. A maximum of 260 nmol·h $^{-1}\cdot g^{-1}$ is reached, but it decreases more rapidly to 90 nmol·h $^{-1}\cdot g^{-1}$ in 24 h. This translates to the total production in 24 h being very similar for both platinum percentages. For 0.35% Pt, it is 3.23 μ mol·g $^{-1}$, and for 0.70% Pt, it is 3.35 μ mol·g $^{-1}$. Hydrogen production is higher than for 0.35%Pt. In this case, a maximum of 8.7 μ mol·h $^{-1}\cdot g^{-1}$ is reached in 1.2 h, which then decreases very randomly. At 24 h, the flow is 3 μ mol·h $^{-1}\cdot g^{-1}$.

In the case of maintaining the platinum percentage at 0.70% and increasing the catalyst load, a higher methane maximum is observed, reaching 470 nmol·h $^{-1}$ ·g $^{-1}$ in 1.5 h and decreasing to 129 nmol·h $^{-1}$ ·g $^{-1}$ at 24 h, with a total production of 5.42 µmol·g $^{-1}$. The hydrogen flow reaches a maximum of 11.27 µmol·h $^{-1}$ ·g $^{-1}$ shortly before the 1 h mark and gradually decreases to 1.2 µmol·h $^{-1}$ ·g $^{-1}$. Both overall productions are lower than those obtained with P25-0.70%Pt. Thus, for methane, we have 5.42 µmol·g $^{-1}$ vs. 7.88 µmol·g $^{-1}$, and for hydrogen, we have 68.93 µmol·g $^{-1}$ vs. 89.67 µmol·g $^{-1}$. This shows the superiority of the P25 in terms of activity compared to the P90. This superiority over other commercial catalysts is usually attributed to its ability to reduce the recombination rate of photogenerated charges due to its crystalline phase composition [86,87].

Although the deposition of Au, like with P25, resulted in lower methane production, in this case, hydrogen formation was not observed, and the formation of a C2 hydrocarbon, ethane, was evidenced at certain times.

Photochem **2025**, 5, 30 14 of 18

With respect to the MB, both for P90-0.70%Pt and P90-0.70%Au, it is eliminated, with mineralization rates of 92% and 51%, respectively, compared to 72% and 49% for the P25 modified to $4~\rm g\cdot L^{-1}$.

4. Conclusions

This work demonstrates, as a viable alternative, the simultaneous removal of a contaminant through the process of carbon dioxide photoreduction. Methylene blue (MB) is a toxic and non-biodegradable contaminant that was efficiently removed and mineralized under the anaerobic conditions required for the photoreduction of carbon dioxide.

Under the evaluated conditions, unmodified P25 did not have sufficient capacity to promote CO₂ photoreduction on its own. Surface metal deposits were therefore added to improve charge separation. Of the three metals tested, namely Pt, Au, and Pd, Pt proved to be the most effective for CH₄ production, followed by Au, while Pd showed the lowest efficiency and evidence of changes in the kinetics and mechanism of the process.

Variables such as pH (3, 5, and 7), catalyst load (2 g·L $^{-1}$ and 4 g·L $^{-1}$), Pt load (0.35% and 0.70%), and MB concentration (20 ppm, 50 ppm, and 100 ppm) were optimized, with the best conditions being pH 5, 0.70% Pt, and 20 ppm MB. The effect of catalyst load should be further investigated, taking into account reactor design conditions.

With respect to the pH levels, pH 5 was the most favorable despite the cationic nature of MB and its low adsorption. It is a pH at which the electrostatic repulsion between the catalyst surface and the MB is reduced compared to pH 3. It also maintains a moderate concentration of bicarbonate ions in the medium compared to that found at higher pH levels, which may contribute to a better approach of the MB to the catalyst surface. At higher pH levels, the excess bicarbonate ions create very high competition for the active sites.

It seems that increasing the load of metallic nanoparticles from 0.35 wt% to 0.70 wt% prevents surface recombination processes and alters the selectivity of the process by modifying the methane/hydrogen ratio.

The P90 exhibited different behavior compared to the P25, with small amounts of C2 hydrocarbons being observed for P90-0.70%Au. In any case, P25 demonstrated its superiority in terms of photocatalytic activity, which can be attributed to its crystalline structure. This shows that the higher specific surface area of the P90 compared to the P25 is not decisive.

In short, the results with TiO_2 -based catalysts are promising, and the use of contaminants as sacrificial agents presents itself as a good environmental alternative. However, more in-depth studies are required on the role of MB in order to increase the overall efficiency of the process. The role that bicarbonate ions seem to play in facilitating the approach of the cationic dye in question towards the surface of these catalysts is interesting. Such studies will be the focus of future work.

Supplementary Materials: The following supporting information can be downloaded at: https://www.mdpi.com/article/10.3390/photochem5040030/s1, Figure S1: FTIR spectra of P25-0.35%Pt with MB at different pH: (a) pH 3, (b) pH 5, (c) pH 7, (d) pH 9, and (e) pH 12.

Author Contributions: E.P.-M.—conceptualization, methodology, formal analysis, investigation, data curation, project administration, writing—original draft preparation, writing—review and editing, supervision, and funding acquisition; C.V.S.-F.—formal analysis, investigation, data curation, and writing—original draft preparation; J.A.—conceptualization, methodology, investigation, data curation, and supervision; Ó.M.G.-D.—conceptualization, data curation, validation, methodology, formal analysis, investigation, writing—original draft preparation, writing—review and editing, and funding acquisition. All authors have read and agreed to the published version of the manuscript.

Photochem **2025**, 5, 30 15 of 18

Funding: This research was financially supported by the State Research Agency of the Spanish Ministry of Science, Innovation, and Universities (MICIU), project reference PID2020-118720RB-I00/AEI/10.13039/501100011033.

Data Availability Statement: The data are contained within the article and the Supplementary Materials. Further inquiries can be directed to the corresponding authors.

Conflicts of Interest: The authors declare no conflicts of interest.

References

- 1. Singla, Y.; Thakur, A.; Sud, D. A comprehensive review on carbon capturing materials and processes for sustainable development. *Mater. Today Energy* **2025**, *48*, 101783. [CrossRef]
- 2. Park, J.H.; Yang, J.; Kim, D.; Gim, H.; Choi, W.Y.; Lee, J.W. Review of recent technologies for transforming carbon dioxide to carbon materials. *Chem. Eng. J.* 2022, 427, 130980. [CrossRef]
- 3. Halmann, M. Photoelectrochemical reduction of aqueous carbon dioxide on p-type gallium phosphide in liquid junction solar cells. *Nature* **1978**, 275, 115–116. [CrossRef]
- 4. Inoue, T.; Fujishima, A.; Konishi, S.; Honda, K. Photoelectrocatalytic reduction of carbon dioxide in aqueous suspensions of semiconductor powders. *Nature* **1979**, 277, 637–638. [CrossRef]
- 5. Lin, C.; Rohilla, J.; Kuo, H.; Chen, C.; Mark Chang, T.; Sone, M.; Ingole, P.P.; Lo, Y.; Hsu, Y. Density-Functional Theory Studies on Photocatalysis and Photoelectrocatalysis: Challenges and Opportunities. *Sol. RRL* **2024**, *8*, 2300948. [CrossRef]
- 6. Chen, C.; Wu, M.; Xu, Y.; Ma, C.; Song, M.; Jiang, G. Efficient Photoreduction of CO₂ to CO with 100% Selectivity by Slowing Down Electron Transport. *J. Am. Chem. Soc.* **2024**, *146*, 9163–9171. [CrossRef] [PubMed]
- 7. Feng, X.; Pi, Y.; Song, Y.; Brzezinski, C.; Xu, Z.; Lin, W. Metal–Organic Frameworks Significantly Enhance Photocatalytic Hydrogen Evolution and CO₂ Reduction with Earth-Abundant Copper Photosensitizers. *J. Am. Chem. Soc.* **2020**, *142*, 690–695. [CrossRef]
- 8. Xue, J.; Jia, X.; Sun, Z.; Li, H.; Shen, Q.; Liu, X.; Jia, H.; Zhu, Y. Selective CO₂ photoreduction to C2 hydrocarbon via synergy between metastable ordered oxygen vacancies and hydrogen spillover over TiO₂ nanobelts. *Appl. Catal. B Environ.* **2024**, 342, 123372. [CrossRef]
- 9. Zhu, Z.; Wang, W.; Li, H.; Zhao, J.; Tang, X. Carbon Nitride and Its Hybrid Photocatalysts for CO₂ Reduction C1 Product Selectivity. *Catalysts* **2025**, *15*, 408. [CrossRef]
- 10. Yuan, Z.; Zhu, X.; Gao, X.; An, C.; Wang, Z.; Zuo, C.; Dionysiou, D.D.; He, H.; Jiang, Z. Enhancing photocatalytic CO₂ reduction with TiO₂-based materials: Strategies, mechanisms, challenges, and perspectives. *Environ. Sci. Ecotechnol.* **2024**, 20, 100368. [CrossRef]
- 11. Zhang, Q.H.; Han, W.D.; Hong, Y.J.; Yu, J.G. Photocatalytic reduction of CO₂ with H₂O on Pt-loaded TiO₂ catalyst. *Catal. Today* **2009**, *148*, 335–340. [CrossRef]
- Nabil, S.; Shalaby, E.A.; Elkady, M.F.; Matsushita, Y.; El-Shazly, A.H. Optimizing the Performance of the Meso-Scale Continuous-Flow Photoreactor for Efficient Photocatalytic CO2 Reduction with Water Over Pt/TiO₂/RGO Composites. Catal. Lett. 2022, 152, 3243–3258. [CrossRef]
- 13. Pougin, A.; Dodekatos, G.; Dilla, M.; Tüysüz, H.; Strunk, J. Au@TiO₂ Core–Shell Composites for the Photocatalytic Reduction of CO₂. *Chem.—A Eur. J.* **2018**, 24, 12416–12425. [CrossRef] [PubMed]
- 14. Yu, S.; Wilson, A.J.; Heo, J.; Jain, P.K. Plasmonic Control of Multi-Electron Transfer and C–C Coupling in Visible-Light-Driven CO₂ Reduction on Au Nanoparticles. *Nano Lett.* **2018**, *18*, 2189–2194. [CrossRef]
- 15. Su, K.Y.; Chen, C.Y.; Wu, R.J. Preparation of Pd/TiO₂ nanowires for the photoreduction of CO₂ into renewable hydrocarbon fuels. *J. Taiwan Inst. Chem. Eng.* **2019**, *96*, 409–418. [CrossRef]
- 16. Liao, G.; Ding, G.; Yang, B.; Li, C. Challenges in Photocatalytic Carbon Dioxide Reduction. *Precis. Chem.* 2024, 2, 49–56. [CrossRef]
- 17. Das, R.; Chakraborty, S.; Peter, S.C. Systematic Assessment of Solvent Selection in Photocatalytic CO₂ Reduction. *ACS Energy Lett.* **2021**, *6*, 3270–3274. [CrossRef]
- 18. Yoshino, S.; Iwase, A.; Yamaguchi, Y.; Suzuki, T.M.; Morikawa, T.; Kudo, A. Photocatalytic CO₂ Reduction Using Water as an Electron Donor under Visible Light Irradiation by Z-Scheme and Photoelectrochemical Systems over (CuGa)_{0.5}ZnS₂ in the Presence of Basic Additives. *J. Am. Chem. Soc.* **2022**, *144*, 2323–2332. [CrossRef] [PubMed]
- 19. Yang, X.; Xiao, T.; Edwards, P.P. The use of products from CO₂ photoreduction for improvement of hydrogen evolution in water splitting. *Int. J. Hydrogen Energy* **2011**, *36*, 6546–6552. [CrossRef]
- 20. Wang, W.; Deng, C.; Xie, S.; Li, Y.; Zhang, W.; Sheng, H.; Chen, C.; Zhao, J. Photocatalytic C–C Coupling from Carbon Dioxide Reduction on Copper Oxide with Mixed-Valence Copper(I)/Copper(II). *J. Am. Chem. Soc.* **2021**, *143*, 2984–2993. [CrossRef]

21. Neamsung, W.; Kitjanukit, N.; Karawek, A.; Chongkol, N.; Lertthanaphol, N.; Chotngamkhum, P.; Khumsupa, K.; Phadungbut, P.; Jonglertjunya, W.; Kim-Lohsoontorn, P.; et al. Effects of alkanolamines on photocatalytic reduction of carbon dioxide to liquid fuels using a copper-doped dititanate/graphene photocatalyst. *RSC Sustain.* **2025**, *3*, 3520–3529. [CrossRef]

- 22. Bratovčić, A.; Tomašić, V. Design and Development of Photocatalytic Systems for Reduction of CO2 into Valuable Chemicals and Fuels. *Processes* **2023**, *11*, 1433. [CrossRef]
- 23. Chávez-Caiza, J.; Fernández-Catalá, J.; Navlani-García, M.; Lousada, C.M.; Berenguer-Murcia, Á.; Cazorla-Amorós, D. Unveiling the effect of sacrificial agent amount in the CO₂ photoreduction performed in a flow reactor. *J. CO2 Util.* **2024**, *83*, 102818. [CrossRef]
- Liu, N.; Tang, M.; Wu, J.; Tang, L.; Huang, W.; Li, Q.; Lei, J.; Zhang, X.; Wang, L. Boosting Visible-Light Photocatalytic Performance for CO₂ Reduction via Hydroxylated Graphene Quantum Dots Sensitized MIL-101(Fe). *Adv. Mater. Interfaces* 2020, 7, 2000468.
 [CrossRef]
- 25. Chen, Y.X.; Xu, Y.F.; Wang, X.D.; Chen, H.Y.; Kuang, D.B. Solvent selection and Pt decoration towards enhanced photocatalytic CO₂ reduction over CsPbBr₃ perovskite single crystals. *Sustain. Energy Fuels* **2020**, *4*, 2249–2255. [CrossRef]
- 26. Park, H.; Ou, H.H.; Kang, U.; Choi, J.; Hoffmann, M.R. Photocatalytic conversion of carbon dioxide to methane on TiO₂/CdS in aqueous isopropanol solution. *Catal. Today* **2016**, 266, 153–159. [CrossRef]
- 27. Liu, Z.; Li, J.; Chen, Z.; Li, M.; Wang, L.; Wu, S.; Zhang, J. Photocatalytic conversion of carbon dioxide on triethanolamine: Unheeded catalytic performance of sacrificial agent. *Appl. Catal. B Environ.* **2023**, *326*, 122338. [CrossRef]
- 28. Liu, Z.; Zhang, J.; Li, X.; Cui, R.; Ma, J.; Sun, R. Simultaneous photocatalytic biomass conversion and CO₂ reduction over high crystalline oxygen-doped carbon nitride. *IScience* **2023**, *26*, 107416. [CrossRef] [PubMed]
- 29. Din, M.I.; Khalid, R.; Najeeb, J.; Hussain, Z. Fundamentals and photocatalysis of methylene blue dye using various nanocatalytic assemblies- a critical review. *J. Clean. Prod.* **2021**, 298, 126567. [CrossRef]
- 30. Khan, I.; Saeed, K.; Zekker, I.; Zhang, B.; Hendi, A.H.; Ahmad, A.; Ahmad, S.; Zada, N.; Ahmad, H.; Shah, L.A.; et al. Review on Methylene Blue: Its Properties, Uses, Toxicity and Photodegradation. *Water* 2022, 14, 242. [CrossRef]
- 31. Oladoye, P.O.; Ajiboye, T.O.; Omotola, E.O.; Oyewola, O.J. Methylene blue dye: Toxicity and potential elimination technology from wastewater. *Results Eng.* **2022**, *16*, 100678. [CrossRef]
- 32. *ISO 10678*; Fine Ceramics (Advanced Ceramics, Advanced Technical Ceramics)—Determination of Photocatalytic Activity of Surfaces in an Aqueous Medium by Degradation of Methylene Blue. ISO: Geneva, Switzerland, 2010.
- 33. Lee, S.K.; Mills, A.; Wells, N. Assessing photocatalytic activity using methylene blue without dye sensitisation. *Catal. Today* **2018**, 313, 211–217. [CrossRef]
- 34. Hernández Rodríguez, M.J.; Pulido Melián, E.; González Díaz, O.; Araña, J.; Macías, M.; González Orive, A.; Doña Rodríguez, J.M. Comparison of supported TiO₂ catalysts in the photocatalytic degradation of NOx. *J. Mol. Catal. A Chem.* **2016**, 413, 56–66. [CrossRef]
- 35. Hernández Rodríguez, M.J.; Pulido Melián, E.; Araña, J.; Navío, J.A.; González Díaz, O.M.; Santiago, D.E.; Doña Rodríguez, J.M. Influence of Water on the Oxidation of NO on Pd/TiO₂ Photocatalysts. *Nanomaterials* **2020**, *10*, 2354. [CrossRef]
- 36. Melián, E.P.; López, C.R.; Méndez, A.O.; Díaz, O.G.; Suárez, M.N.; Doña Rodríguez, J.M.; Navío, J.A.; Fernández Hevia, D. Hydrogen production using Pt-loaded TiO₂ photocatalysts. *Int. J. Hydrogen Energy* **2013**, *38*, 11737–11748. [CrossRef]
- 37. Ortega Méndez, J.A.; López, C.R.; Pulido Melián, E.; González Díaz, O.; Doña Rodríguez, J.M.; Fernández Hevia, D.; Macías, M. Production of hydrogen by water photo-splitting over commercial and synthesised Au/TiO₂ catalysts. *Appl. Catal. B Environ.* **2014**, 147, 439–452. [CrossRef]
- 38. Mohamed, R.M.; Ismail, A.A.; Kadi, M.W.; Bahnemann, D.W. A comparative study on mesoporous and commercial TiO₂ photocatalysts for photodegradation of organic pollutants. *J. Photochem. Photobiol.* **2018**, *367*, 66–73. [CrossRef]
- 39. Thirunavukkarasu, G.K.; Bacova, J.; Monfort, O.; Dworniczek, E.; Paluch, E.; Hanif, M.B.; Rauf, S.; Motlochova, M.; Capek, J.; Hensel, K.; et al. Critical comparison of aerogel TiO₂ and P25 nanopowders: Cytotoxic properties, photocatalytic activity and photoinduced antimicrobial/antibiofilm performance. *Appl. Surf. Sci.* **2022**, *579*, 152145. [CrossRef]
- 40. Sangchay, W.; Sikong, L.; Kooptarnond, K. Comparison of photocatalytic reaction of commercial P25 and synthetic TiO₂-AgCl nanoparticles. *Procedia Eng.* **2012**, *32*, 590–596. [CrossRef]
- 41. Soleimani, M.; Boorboor Azimi, E.; Mousavi, M.; Ghasemi, J.B.; Badiei, A. The first study of adsorption of methylene blue by Black Titania nanoparticle in aqueous solution. *Sci. Iran.* **2022**, *30*, 2001–2010. [CrossRef]
- 42. Zeng, M. Influence of TiO₂ Surface Properties on Water Pollution Treatment and Photocatalytic Activity. *Bull. Korean Chem. Soc.* **2013**, *34*, 953–956. [CrossRef]
- 43. Niu, L.; Zhao, X.; Tang, Z.; Lv, H.; Wu, F.; Wang, X.; Zhao, T.; Wang, J.; Wu, A.; Giesy, J.P. Difference in performance and mechanism for methylene blue when TiO₂ nanoparticles are converted to nanotubes. *J. Clean. Prod.* **2021**, 297, 126498. [CrossRef]
- 44. Ovchinnikov, O.V.; Evtukhova, A.V.; Kondratenko, T.S.; Smirnov, M.S.; Khokhlov, V.Y.; Erina, O.V. Manifestation of intermolecular interactions in FTIR spectra of methylene blue molecules. *Vib. Spectrosc.* **2016**, *86*, 181–189. [CrossRef]

Photochem **2025**, 5, 30 17 of 18

45. Alver, E.; Metin, A.Ü.; Brouers, F. Methylene blue adsorption on magnetic alginate/rice husk bio-composite. *Int. J. Biol. Macromol.* **2020**, *154*, 104–113. [CrossRef]

- 46. Khnifira, M.; El Hamidi, S.; Mahsoune, A.; Sadiq, M.; Serdaroğlu, G.; Kaya, S.; Qourzal, S.; Barka, N.; Abdennouri, M. Adsorption of methylene blue cationic dye onto brookite and rutile phases of titanium dioxide: Quantum chemical and molecular dynamic simulation studies. *Inorg. Chem. Commun.* **2021**, *129*, 108659. [CrossRef]
- 47. Sabnis, R.W. *Handbook of Biological Dyes and Stains: Synthesis and Industrial Applications*; John Wiley & Sons, Inc.: Hoboken, NJ, USA, 2010; pp. 293–297. [CrossRef]
- 48. Saleem, M.; Choi, N.G.; Lee, K.H. Facile synthesis of an optical sensor for CO₃²⁻ and HCO₃⁻ detection. *Int. J. Environ. Anal. Chem.* **2015**, 95, 592–608. [CrossRef]
- 49. Bouziani, M.; Bouziani, A.; Hsini, A.; Bianchi, C.L.; Falletta, E.; Di Michele, A.; Çelik, G.; Hausler, R. Synergistic photocatalytic degradation of methylene blue and ibuprofen using Co₃O₄-Decorated hexagonal boron nitride (hBN) composites under Sun-like irradiation. *Chemosphere* **2025**, *371*, 144061. [CrossRef]
- 50. Minamoto, C.; Fujiwara, N.; Shigekawa, Y.; Tada, K.; Yano, J.; Yokoyama, T.; Minamoto, Y.; Nakayama, S. Effect of acidic conditions on decomposition of methylene blue in aqueous solution by air microbubbles. *Chemosphere* **2021**, 263, 128141. [CrossRef]
- 51. Chen, H.Y.; Zahraa, O.; Bouchy, M. Inhibition of the adsorption and photocatalytic degradation of an organic contaminant in an aqueous suspension of TiO₂ by inorganic ions. *J. Photochem. Photobiol. A Chem.* **1997**, *108*, 37–44. [CrossRef]
- 52. Gao, X.; Guo, Q.; Tang, G.; Peng, W.; Luo, Y.; He, D. Effects of inorganic ions on the photocatalytic degradation of carbamazepine. *J. Water Reuse Desalin.* **2019**, *9*, 301–309. [CrossRef]
- 53. Ghosh, S.; Sahu, M. Insights on the influence of natural co-contaminants on the photocatalytic performance of biochar supported p-n heterojunction photocatalyst in an aqueous media. *Clean. Water* **2025**, *4*, 100089. [CrossRef]
- 54. Li, X.; Raza, S.; Liu, C. Directly electrospinning synthesized Z-scheme heterojunction TiO₂@Ag@Cu₂O nanofibers with enhanced photocatalytic degradation activity under solar light irradiation. *J. Environ. Chem. Eng.* **2021**, *9*, 106133. [CrossRef]
- 55. Kalaycioglu, Z.; Uysal, B.Ö.; Pekcan, Ö.; Erim, F.B. Efficient photocatalytic degradation of methylene blue dye from aqueous solution with cerium oxide nanoparticles and graphene oxide-doped polyacrylamide. *ACS Omega* **2023**, *8*, 13004–13015. [CrossRef]
- 56. Baran, T.; Caringella, D.; Dibenedetto, A.; Aresta, M. Pitfalls in Photochemical and Photoelectrochemical Reduction of CO₂ to Energy Products. *Molecules* **2024**, *29*, 4758. [CrossRef]
- 57. Zhai, Q.; Xie, S.; Fan, W.; Zhang, Q.; Wang, Y.; Deng, W.; Wang, Y. Photocatalytic Conversion of Carbon Dioxide with Water into Methane: Platinum and Copper(I) Oxide Co-catalysts with a Core–Shell Structure. *Angew. Chem. Int. Ed.* **2013**, 52, 5776–5779. [CrossRef] [PubMed]
- 58. Cheng, L.; Wu, C.; Feng, H.; Liu, H. Sacrificial agent-free photocatalytic CO₂ reduction using a 2D cobalt porphyrin-based MOF/graphene heterojunction. *Catal. Sci. Technol.* **2022**, *12*, 7057–7064. [CrossRef]
- 59. Coenen, K.; Gallucci, F.; Mezari, B.; Hensen, E.; van Sint Annaland, M. An in-situ IR study on the adsorption of CO₂ and H₂O on hydrotalcites. *J. CO2 Util.* **2018**, 24, 228–239. [CrossRef]
- 60. Prescott, H.; Li, Z.; Kemnitz, E.; Trunschke, A.; Deutsch, J.; Lieske, H.; Auroux, A. Application of calcined Mg–Al hydrotalcites for Michael additions: An investigation of catalytic activity and acid–base properties. *J. Catal.* **2005**, 234, 119–130. [CrossRef]
- 61. Venkatesvaran, H.; Balu, S.; Yang, W.; Chiu, P.W.; Juodkazytė, J.; Yang, T.C.K.; Lee, Y.C. Operando DRIFTS investigation of CO₂ hydrogenation over Pd nanoparticle-deposited P90-TiO₂–x. *J. Environ. Chem. Eng.* **2025**, *13*, 117312. [CrossRef]
- 62. AlMohamadi, H.; Awad, S.A.; Sharma, A.K.; Fayzullaev, N.; Távara-Aponte, A.; Chiguala-Contreras, L.; Amari, A.; Rodriguez-Benites, C.; Tahoon, M.A.; Esmaeili, H. Photocatalytic Activity of Metal- and Non-Metal-Anchored ZnO and TiO₂ Nanocatalysts for Advanced Photocatalysis: Comparative Study. *Catalysts* **2024**, *14*, 420. [CrossRef]
- 63. Paul, D.R.; Sharma, R.; Nehra, S.P.; Sharma, A. Effect of calcination temperature, pH and catalyst loading on photodegradation efficiency of urea derived graphitic carbon nitride towards methylene blue dye solution. *RSC Adv.* **2019**, *9*, 15381–15391. [CrossRef]
- 64. Pellegrino, F.; Pellutiè, L.; Sordello, F.; Minero, C.; Ortel, E.; Hodoroaba, V.D.; Maurino, V. Influence of agglomeration and aggregation on the photocatalytic activity of TiO₂ nanoparticles. *Appl. Catal. B Environ.* **2017**, *216*, 80–87. [CrossRef]
- 65. Dou, Y.; Zhou, A.; Yao, Y.; Lim, S.Y.; Li, J.R.; Zhang, W. Suppressing hydrogen evolution for high selective CO₂ reduction through surface-reconstructed heterojunction photocatalyst. *Appl. Catal. B Environ.* **2021**, *286*, 119876. [CrossRef]
- 66. Katsumata, K.; Sakai, K.; Ikeda, K.; Carja, G.; Matsushita, N.; Okada, K. Preparation and photocatalytic reduction of CO₂ on noble metal (Pt, Pd, Au) loaded Zn–Cr layered double hydroxides. *Mater. Lett.* **2013**, *107*, 138–140. [CrossRef]
- 67. Pulido Melián, E.; Henríquez-Cárdenes, E.; González Díaz, O.; Doña Rodríguez, J.M. Study of adsorption and degradation of dimethylphthalate on TiO₂-based photocatalysts. *Chem. Phys.* **2016**, 475, 112–118. [CrossRef]
- 68. Mondal, S.; De Anda Reyes, M.E.; Pal, U. Plasmon induced enhanced photocatalytic activity of gold loaded hydroxyapatite nanoparticles for methylene blue degradation under visible light. *RSC Adv.* **2017**, *7*, 8633–8645. [CrossRef]
- 69. Wang, X.; Han, S.; Zhang, Q.; Zhang, N.; Zhao, D. Photocatalytic oxidation degradation mechanism study of methylene blue dye waste water with GR/iTO 2. *MATEC Web Conf.* **2018**, 238, 03006. [CrossRef]

Photochem **2025**, 5, 30 18 of 18

70. Conte, F.; Rossetti, I.; Ramis, G.; Vaulot, C.; Hajjar-Garreau, S.; Bennici, S. Low Metal Loading (Au, Ag, Pt, Pd) Photo-Catalysts Supported on TiO₂ for Renewable Processes. *Materials* **2022**, *15*, 2915. [CrossRef]

- 71. Zuo, C.; Su, Q.; Yan, X. Research Progress of Co-Catalysts in Photocatalytic CO₂ Reduction: A Review of Developments, Opportunities, and Directions. *Processes* **2023**, *11*, 867. [CrossRef]
- 72. Han, Y.; Xu, H.; Su, Y.; Xu, Z.; Wang, K.; Wang, W. Noble metal (Pt, Au@Pd) nanoparticles supported on metal organic framework (MOF-74) nanoshuttles as high-selectivity CO₂ conversion catalysts. *J. Catal.* **2019**, *370*, *70*–78. [CrossRef]
- 73. Tian, J.; Zhong, K.; Zhu, X.; Yang, J.; Mo, Z.; Liu, J.; Dai, J.; She, Y.; Song, Y.; Li, H.; et al. Highly exposed active sites of Au nanoclusters for photocatalytic CO₂ reduction. *Chem. Eng. J.* **2023**, *451*, 138392. [CrossRef]
- 74. Yadav, M.; Basheer, H.S.; Ágfalvi, Á.; Ábrahámné, K.B.; Kiss, J.; Halasi, G.; Sápi, A.; Kukovecz, Á.; Kónya, Z. Noble metals-deposited TiO₂ photocatalysts for photoreduction of CO₂: Exploration of surface chemistry and a reflection on the importance of wavelength dependence. Appl. Catal. A Gen. 2023, 668, 119434. [CrossRef]
- 75. Liu, Q.; Bai, C.; Zhu, C.; Guo, W.; Li, G.; Guo, S.; Kripalani, D.; Zhou, K.; Chen, R. M/BiOCl-(M = Pt, Pd, and Au) Boosted Selective Photocatalytic CO₂ Reduction to C₂ Hydrocarbons via *CHO Intermediate Manipulation. *Adv. Sci.* **2024**, *11*, 2400934. [CrossRef]
- 76. Tanaka, K.; White, J.M. Dissociative adsorption of carbon dioxide on oxidized and reduced platinum/titanium dioxide. *J. Phys. Chem.* **1982**, *86*, 3977–3980. [CrossRef]
- 77. López, C.R.; Melián, E.P.; Ortega Méndez, J.A.; Santiago, D.E.; Doña Rodríguez, J.M.; González Díaz, O. Comparative study of alcohols as sacrificial agents in H₂ production by heterogeneous photocatalysis using Pt/TiO₂ catalysts. *J. Photochem. Photobiol. A Chem.* 2015, 312, 45–54. [CrossRef]
- 78. Khan, N.; Sapi, A.; Arora, I.; Sagadevan, S.; Chandra, A.; Garg, S. Photocatalytic CO₂ reduction using metal and nonmetal doped TiO₂ and its mechanism. *React. Kinet. Mech. Catal.* **2024**, 137, 629–655. [CrossRef]
- 79. Kreft, S.; Schoch, R.; Schneidewind, J.; Rabeah, J.; Kondratenko, E.V.; Kondratenko, V.A.; Junge, H.; Bauer, M.; Wohlrab, S.; Beller, M. Improving Selectivity and Activity of CO₂ Reduction Photocatalysts with Oxygen. *Chem* **2019**, *5*, 1818–1833. [CrossRef]
- 80. Kharade, A.K.; Chang, S. Contributions of Abundant Hydroxyl Groups to Extraordinarily High Photocatalytic Activity of Amorphous Titania for CO₂ Reduction. *J. Phys. Chem. C* **2020**, 124, 10981–10992. [CrossRef]
- 81. Han, C.; Lei, Y.; Wang, B.; Wu, C.; Zhang, X.; Shen, S.; Sun, L.; Tian, Q.; Feng, Q.; Wang, Y. The functionality of surface hydroxyls on selective CH₄ generation from photoreduction of CO₂ over SiC nanosheets. *Chem. Commun.* **2019**, *55*, 1572–1575. [CrossRef]
- 82. Yu, H.; Yan, S.; Zhou, P.; Zou, Z. CO₂ photoreduction on hydroxyl-group-rich mesoporous single crystal TiO₂. *Appl. Surf. Sci.* **2018**, 427, 603–607. [CrossRef]
- 83. Banerjee, S.; Zangiabadi, A.; Mahdavi-Shakib, A.; Husremovic, S.; Frederick, B.G.; Barmak, K.; Austin, R.N.; Billinge, S.J.L. Quantitative Structural Characterization of Catalytically Active TiO₂ Nanoparticles. *ACS Appl. Nano Mater.* **2019**, *2*, 6268–6276. [CrossRef]
- 84. Chen, Y.; Soler, L.; Armengol-Profitós, M.; Xie, C.; Crespo, D.; Llorca, J. Enhanced photoproduction of hydrogen on Pd/TiO₂ prepared by mechanochemistry. *Appl. Catal. B Environ.* **2022**, 309, 121275. [CrossRef]
- 85. Dontsova, T.A.; Yanushevska, O.I.; Nahirniak, S.V.; Kutuzova, A.S.; Krymets, G.V.; Smertenko, P.S. Characterization of Commercial TiO₂ P90 Modified with ZnO by the Impregnation Method. *J. Chem.* **2021**, 2021, 9378490. [CrossRef]
- 86. Collado, L.; García-Tecedor, M.; Gomez-Mendoza, M.; Pizarro, A.H.; Oropeza, F.E.; Liras, M.; de la Peña O'Shea, V.A. Unravelling charge dynamic effects in photocatalytic CO₂ reduction over TiO₂: Anatase vs P25. *Catal. Today* **2023**, 423, 114279. [CrossRef]
- 87. Hurum, D.C.; Agrios, A.G.; Gray, K.A.; Rajh, T.; Thurnauer, M.C. Explaining the Enhanced Photocatalytic Activity of Degussa P25 Mixed-Phase TiO₂ Using EPR. *J. Phys. Chem. B* **2003**, *107*, 4545–4549. [CrossRef]

Disclaimer/Publisher's Note: The statements, opinions and data contained in all publications are solely those of the individual author(s) and contributor(s) and not of MDPI and/or the editor(s). MDPI and/or the editor(s) disclaim responsibility for any injury to people or property resulting from any ideas, methods, instructions or products referred to in the content.